




Monte Carlo simulation of a lattice model for the dynamics of randomly branching double-folded ring polymers

Elham Ghobadpour ^{1,2}, Max Kolb,³ Mohammad Reza Ejtehadi ⁴, and Ralf Everaers ^{3,*}

¹Université Grenoble Alpes, Centre National de la Recherche Scientifique (CNRS), TIMC, F-38000 Grenoble, France

²School of Nano Science, Institute for Research in Fundamental Sciences (IPM), 19395-5531, Tehran, Iran

³Université de Lyon, École Normale Supérieure (ENS) de Lyon, CNRS,

Laboratoire de Physique and Centre Blaise Pascal de l'ENS de Lyon, F-69342 Lyon, France

⁴Department of Physics, Sharif University of Technology, 11155-9161, Tehran, Iran



(Received 19 January 2020; revised 27 April 2021; accepted 7 June 2021; published 13 July 2021)

Supercoiled DNA, crumpled interphase chromosomes, and topologically constrained ring polymers often adopt treelike, double-folded, randomly branching configurations. Here we study an elastic lattice model for tightly double-folded ring polymers, which allows for the spontaneous creation and deletion of side branches coupled to a diffusive mass transport, which is local both in space and on the connectivity graph of the tree. We use Monte Carlo simulations to study systems falling into three different universality classes: ideal double-folded rings without excluded volume interactions, self-avoiding double-folded rings, and double-folded rings in the melt state. The observed static properties are in good agreement with exact results, simulations, and predictions of Flory theory for randomly branching polymers. For example, in the melt state rings adopt compact configurations and exhibit territorial behavior. In particular, we show that the emergent dynamics is in excellent agreement with a recent scaling theory and illustrate the qualitative differences with the familiar reptation dynamics of linear chains.

DOI: [10.1103/PhysRevE.104.014501](https://doi.org/10.1103/PhysRevE.104.014501)

I. INTRODUCTION

The behavior of melts of nonconcatenated ring polymers has caught the interest of physicists over many years [1–12] and appears to provide a natural explanation for the territorial chromosomal arrangement in eukaryotic cells during interphase [13–15]. With their microscopic topological state permanently quenched, the equilibrium statistics and dynamics of nonconcatenated ring polymers is fundamentally different from the behavior of their linear counterparts. A powerful approximation is available through the analogy with ring polymers in an array of fixed obstacles [1,3,7,8]. In this view, crumpling can be understood by the successive application of three different strategies for entropy maximization: double folding, branching, and swelling. Firstly, and most importantly, the rings adopt double-folded configurations to minimize the threadable surface, as this reduces the importance of the topological constraints they impose on each other. Secondly, double-folded rings can increase their entropy by branching. Thirdly, there is a certain amount of swelling due to partially screened excluded volume interactions leading to asymptotically compact conformations characterized by the scaling exponent of the radius of gyration, $\nu = 1/d$ for $d \leq 4$ dimensions. Double-folding, branching, and swelling due to excluded volume interactions also occur in plectonemic configurations of supercoiled circular DNA [16–20].

Similarly, viral RNA may effectively behave like branched polymers [21–23]. From a more general perspective, the mapping of (double-folded) ring polymers to randomly branched polymers or trees suggests analogies to phenomena such as gelation [24], percolation [25], and the critical behavior of magnetic systems [26–29]. This may explain, why polymer physics [24,30–32] is often concerned with exponents, which characterize the essence of the behavior of all members of a universality class and are independent of microscopic details differentiating particular experimental polymers as well as lattice and off-lattice models from each other.

Recent numerical work on the *static* properties of self-avoiding trees and lattice tree melts [33–35] has shown that the behavior of randomly branching chains under different solvent conditions is in excellent qualitative agreement with a suitably generalized Flory theory [13,36]. A multiscale approach to the construction of ring melts based on this analogy faithfully captures many aspects of the conformational statistics of properly equilibrated systems [11,12]. However, Monte Carlo algorithms optimized for rapidly equilibrating the static structure of randomly branching chains [37,38] [Fig. 1(c)] generate an artificial dynamics.

To generate a physically more realistic dynamics, Monte Carlo simulations [39–41] need to obey the same conservation laws [42] as the modeled target systems. In the present case, this requires a scheme where the mass transport is local both in space and on the connectivity graph of the tree.

Below we present Monte Carlo simulations of a suitable elastic lattice polymer model which accounts for double folding [4,43], the local accumulation of contour length on the

*ralf.everaers@ens-lyon.fr

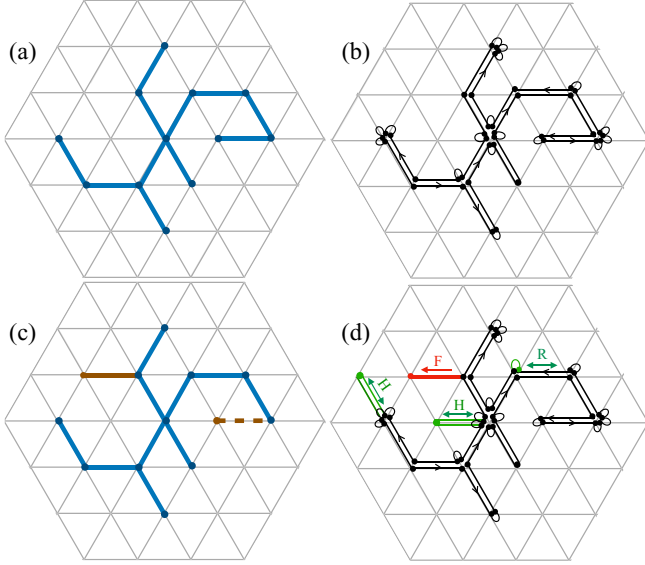


FIG. 1. (a) Branched tree on a trigonal lattice and (b) a corresponding (tightly wrapped) double-folded ring polymer. Small loops represent bonds of zero length, where adjacent monomers along the ring occupy identical lattice sites. (c) Example of a nonlocal “amoeba” Monte Carlo move [37,38] altering the tree structure. The dashed brown line shows the location of a branch prior to the MC move, and the solid brown line shows an arbitrary location where the branch could be reattached to the tree. (d) Examples of local MC moves for the present model of double-folded ring polymers. Dots represent monomers, and black lines represent an allowed conformation of the double-folded chain. The allowed (forbidden) moves are indicated by the green (red) color. R: the Repton move. H: the Hairpin move. F: the Forbidden move that does not preserve the double-folded structure.

primitive tree [4,40,44–46], as well as excluded volume interactions [44–46].

The manuscript is structured as follows: In Sec. II we introduce relevant observables and the related exponents. Also, we briefly summarize the theoretical background. The model and the simulations are described in Sec. III. In Sec. IV we present and discuss our results. After some first qualitative insights in Sec. IV A, we validate that the static properties of our model are in good agreement with theoretical and numerical work on trees (Sec. IV B). The next step, Sec. IV C, focuses on comparison of the single ring dynamics with the predictions of a recent scaling theory [3,8]. Furthermore, we compare the dynamics of double-folded rings to the motion of linear chains in the tube model [47] (Sec. IV D). Finally, we briefly conclude in Sec. V.

II. THEORETICAL BACKGROUND

A double-folded ring polymer can be mapped on a randomly branched primitive tree [1,3,4,7,8,11,48,49]. In analogy to protein or RNA structures, such conformations can be discussed in terms of a primary, a secondary, and a tertiary structure [50]. The primary structure is simply defined through the connectivity of the ring monomers. The secondary structure arises from the double folding and can be

specified through the mapping of the ring onto a graph with the connectivity of the primitive tree. The tertiary structure describes the embedding of the rings and trees into (three-dimensional) space. We define corresponding observables in Secs. II A and II B. Sections II C and II D briefly summarize scaling arguments for the effect of excluded volume interactions and the dynamics of randomly branched double-folded ring polymers.

A. Secondary structure

Two standard measures of the tree connectivity are the mean contour distance L between tree nodes and the average weight of branches N_{br} , separated from the tree by severing a randomly chosen link. Both depend on the weight N of the rings through power law relations

$$\langle L(N) \rangle \sim N^\rho, \quad (1)$$

$$\langle N_{\text{br}}(N) \rangle \sim N^\epsilon, \quad (2)$$

where $\epsilon = \rho$ is expected to hold in general [38]. The (tight) wrapping of a tree by a ring polymer introduces an additional metric on the embedded graph [50]. The central quantity is the length of the shortest path on the *tree* or tree contour distance, L , between two monomers i and j along the ring. For short *ring* contour distances, $n = |i - j|$, one simply expects $\langle L(n) \rangle \sim n$. However, beyond the typical distance between branch points, the ring does not follow a linear path on the tree but wraps side branches. For $n \ll N$, Eq. (1) suggests $\langle L(n) \rangle \sim n^\rho$. Due to the ring closure $\langle L(n) \rangle \equiv \langle L(N - n) \rangle$ reaches its maximum for $n = N/2$ before reducing to zero at the total ring size, $\langle L(N) \rangle \equiv 0$. The simplest functional form accounting for this constraint is [50]

$$\langle L(n) \rangle_N \sim \left[n \left(1 - \frac{n}{N} \right) \right]^\rho. \quad (3)$$

B. Tertiary structure

The simplest measures of the tertiary structure are the overall tree gyration radii,

$$\langle R_g^2(N) \rangle \sim N^{2\nu}, \quad (4)$$

as a function of the chain length. For a more detailed understanding, it is useful to consider the mean-square spatial distance between nodes,

$$\langle R^2(L) \rangle \sim L^{2\nu_{\text{path}}}, \quad (5)$$

as a function of their contour distance on the tree, where $\nu = \rho \nu_{\text{path}}$. Combining Eqs. (5) and (3) suggests [50]

$$\langle R^2(n) \rangle_N \sim \left[n \left(1 - \frac{n}{N} \right) \right]^{2\nu} \quad (6)$$

for the mean-square spatial distance of monomers as a function of their distance, $n = |i - j|$, along the ring.

C. Flory theory

Exact values for the exponents are known only for a very small number of cases. For ideal noninteracting trees, the exponents $\rho^{\text{ideal}} = \epsilon^{\text{ideal}} = \nu_{\text{path}}^{\text{ideal}} = 1/2$ and $\nu^{\text{ideal}} = 1/4$ [51,52].

For interacting trees, the only known exact result [26] is the value $\nu = 1/2$ for self-avoiding trees in $d = 3$.

Flory theories [7,13,36,53,54] of interacting tree systems are formulated as a balance of an entropic elastic term and an interaction energy [55]

$$\mathcal{F} = \mathcal{F}_{el}(N, R) + \mathcal{F}_{inter}(N, R). \quad (7)$$

In the present case, the elastic free energy takes the form [13]

$$\frac{\mathcal{F}_{el}}{k_B T} \sim \frac{R^2}{l_K L} + \frac{L^2}{N l_K^2}. \quad (8)$$

The first term of Eq. (8) is the usual elastic energy contribution for stretching a polymer of linear contour length L at its ends [13]. The second term penalizes deviations from the ideal branching statistics, which lead to longer paths and hence spatially more extended trees. Optimizing L for annealed trees for a *given* asymptotic, $R \sim N^\nu$, yields [13,36]

$$\rho = \frac{1 + 2\nu}{3}, \quad (9)$$

$$\nu_{\text{path}} = \frac{3\nu}{1 + 2\nu}, \quad (10)$$

independently of the type of volume interactions causing the swelling in the first place. Plausibly, a fully extended system, $\nu = 1$, is predicted not to branch, $\rho = 1$, and to have a fully stretched stem, $\nu_{\text{path}} = \nu = 1$. For the radius of ideal randomly branched polymers, $\nu = 1/4$, one recovers $\rho = 1/2$ and Gaussian path statistics, $\nu_{\text{path}} = 1/2$.

Reference [36] reviews the predictions of the Flory theory for randomly branching polymers for a wide range of conditions characterized by different expressions for the interaction energy in Eq. (7). For self-avoiding trees, $\frac{\mathcal{F}_{inter}(N,R)}{k_B T} \sim \nu_2 \frac{N^2}{R^d}$ represents the two-body repulsion between segments, which dominates in good solvent. In this case, Flory theory predicts [13]

$$\nu = \frac{7}{3d + 4} \quad 1 \leq d \leq 8, \quad (11)$$

in qualitatively excellent and almost quantitative agreement with the exact results [33]. In dense melts, all terms of the virial expansion of the partially screened excluded volume interactions become relevant and the trees are expected to be compact [36]:

$$\nu = \frac{1}{d} \quad 1 \leq d \leq 4. \quad (12)$$

While Flory theory describes the average behavior of the tree observables mentioned above, we note for completeness that the corresponding non-Gaussian distribution functions are typically of the Redner–des Cloizeaux (RdC) form of a power law multiplied with a stretched exponential. Most of the additional exponents characterizing the tails of the distributions can be related to each other and the standard tree exponents [35,50].

D. Dynamics

In the following we summarize the arguments for the dynamics of randomly branched double-folded ring polymers from Refs. [3,4,8]. Consider the division of a tree into its trunk (the longest path on the tree) and the branches hanging off this

trunk. The trunk has a length of $L \sim aN^\rho$, where a is the lattice constant and the number of branches is proportional to L . The slowest relaxation process is the transport of mass along the trunk, while the intrabranch dynamics is irrelevant and may be neglected [3,4]. The elementary step of the dynamics is the reptonlike exchange of mass between neighboring branches along the trunk [56]. Each elementary event changes the average projected position of the monomers along the trunk by an amount $\delta s_{CM} \sim a/N$. The number of such events by an elementary unit of time τ_0 is proportional to the number of branches. As a consequence, $\langle \delta s_{CM}^2(\tau_0) \rangle \sim (a/N)^2 N^\rho$, corresponding to a diffusion constant for the curvilinear motion along the trunk of $D_{||}(N) \sim \langle \delta s_{CM}^2(\tau_0) \rangle / \tau_0 \sim (a^2/\tau_0) N^{\rho-2}$. To completely relax the internal tree structure, the tree CM has to diffuse over the entire trunk length. As a consequence,

$$\tau_{\text{max}}(N) \sim \frac{(aN^\rho)^2}{(a^2/\tau_0)N^{\rho-2}} \sim \tau_0 N^{\rho+2}, \quad (13)$$

or, using Eq. (9), $\tau_{\text{max}}(N) \sim \tau_0 N^{(7+2\nu)/3}$. As this corresponds to a mean-square spatial displacement of $\langle \delta R_{CM}^2(\tau_{\text{max}}) \rangle \sim \langle R_g^2(N) \rangle \sim a^2 N^{2\nu}$, the long-time CM and monomer diffusion are given by

$$g_{1,3}(t \gg \tau_{\text{max}}(N)) \sim D_{CM}(N) t \quad (14)$$

with

$$D_{CM}(N) \sim \frac{a^2}{\tau_0} N^{2\nu-\rho-2} \quad (15)$$

or $D_{CM}(N) \sim \frac{a^2}{\tau_0} N^{(4\nu-7)/3}$.

Furthermore, one can invert Eq. (13) to obtain the mass,

$$n(t) \sim \left(\frac{t}{\tau_0} \right)^{\frac{1}{\rho+2}}, \quad (16)$$

of rings (or ring sections) which are equilibrated after a given time, $\tau_0 < t < \tau_{\text{max}}$. During a corresponding time interval, monomers move over a spatial distance of the order of $a^2 n(t)^{2\nu}$:

$$g_1(\tau_0 < t < \tau_{\text{max}}) \sim a^2 \left(\frac{t}{\tau_0} \right)^{\frac{2\nu}{\rho+2}}, \quad (17)$$

which is independent of the total ring length. Similarly, one can estimate the CM motion by noting that each of the $n(t)/N$ equilibrated ring sections independently moves over a distance of the order of $a^2 n(t)^{2\nu}$. As a consequence,

$$g_3(\tau_0 < t < \tau_{\text{max}}) \sim g_1(t) \frac{n(t)}{N} \sim \frac{1}{N} a^2 \left(\frac{t}{\tau_0} \right)^{\frac{2\nu+1}{\rho+2}}. \quad (18)$$

III. MODEL AND METHOD

Monte Carlo simulations [39–41] can be expected to generate physically realistic results if they obey the same conservation laws [42] as the modeled target systems. As an illustration in the present context, consider first an algorithm on the tree level, which removes or adds segments with a probability governed by a chemical potential. While this allows control of the *average* tree weight, such an algorithm is clearly inappropriate to simulate (double-folded) ring polymers of *fixed* weight. This difficulty is partially overcome by the amoeba algorithm of Seitz and Klein [37], which attempts to move one-functional tree “leaves” to random locations on

the tree [Fig. 1(c)]. Since this operation conserves the tree weight, the algorithm can be meaningfully employed to study static aspects of the ring polymer and the chromosome folding problem [11,14,34,49]. The same holds true for a variant of the same idea by Janse van Rensburg and Madras [38], which achieves a much higher efficiency in dilute systems by cutting and relocating entire branches. Similarly, one could envision a (probably highly efficient) variant of the connectivity altering double-bridging scheme [57] for tree melts, where neighboring trees swap entire branches of equal weight without moving them in space. Such moves can be expected to have a much higher acceptance probability in dense systems, since they preserve the uniform monomer density. However, none of these algorithms can be used to simulate the configurational *dynamics* of double-folded ring polymers. Instead we require a scheme where *the mass transport is local in space and on the connectivity graph* of the tree.

In the following, we first review the elastic lattice polymer model [40,43–46], which is a simple and efficient Monte Carlo algorithm for studying the dynamics of entangled linear chains (Sec. III A). In Sec. III B we describe the generalization to randomly branching double-folded ring polymers [4]. Sections III C and III D provide more details on the systems studied and on how we initialized and equilibrated our runs.

A. Elastic lattice polymer models

The dynamics of topologically constrained *linear* polymers can be efficiently studied in Monte Carlo (MC) simulations of the coarse-grained elastic lattice polymer model [40,43–46]. In this model the continuum dynamics of a polymer melt is replaced by a lattice version. The mapping is achieved by dividing the space into cells where the centers of these cells form a regular lattice. By moving all the monomers residing in a cell to the center, the polymer conformation and its dynamics are discretized. The maximum number of monomers per site is a free parameter of the model that depends on the coarse graining, e.g., it can be calculated by considering the volume of the monomers and the cell volume. The projection of real space onto a lattice will also limit the dynamics to nearest-neighbor hops of the monomers. As a result of the coarse graining, the only allowed bond lengths between neighboring monomers can be 0 or 1, 0 for monomers that are in the same cell, and 1 for monomers residing in neighboring cells. This also means that any MC move should only be accepted if it preserves this constraint.

In order to guarantee the constraints of excluded volume and noncrossing of strands, without the loss of generality, a minor restraint is introduced to the occupancy of the cells [4]. Multiple occupancy on a lattice site is allowed only for monomers that are directly connected to each other by monomers on the same site, i.e., they form a polymer strand of variable length (a subchain of chemically bonded monomers), where the length of such a strand is limited by the cell size. This also guarantees that monomers belonging to different polymers can never occupy the same site. With this constraint the implementation of excluded volume interaction and noncrossability becomes operationally trivial while fully maintaining a repton [56]-like dynamics along the primitive chain [47].

When the elastic lattice polymer model is used to simulate ring polymers [46,49], the algorithm conserves the microscopic topological state of the starting configuration. In particular, melts of long, nonconcatenated rings exhibit compact and characteristically crumpled conformations.

B. Generalization to randomly branching double-folded ring polymers

When the algorithm is generalized to double-folded polymers [4], lattice bonds represent tree segments which can only be occupied by two oppositely oriented bonds between ring monomers [Fig. 1(b)]. Tree nodes are located on lattice sites. Their functionality depends on the number of emerging tree segments, $f = 1$ (a leaf or branch tip), $f = 2$ (linear chain section), and $f \geq 3$ (branch point). As in the elastic lattice polymer model and in contrast to standard tree models [33,37,38] (which can be wrapped *a posteriori* with ring polymers [50]), the degrees of freedom are the positions of the ring monomers. The local redistribution of stored length is responsible for the dynamics. In contrast to the elastic lattice polymer model, the connectivity graph for the connected lattice sites is a dynamically branching object. In particular, new side branches are created when a monomer from inside an accumulation of stored length moves to a neighboring lattice site. Conversely, side branches vanish when the last monomer reintegrates into the main branch and retracts the two remaining extended ring bonds representing the tree segment [Fig. 1(d)]. Specifically, we impose the following rules:

Lattice: Ring monomers are placed on the sites of a periodic FCC lattice. We choose the FCC lattice because it is isotropic and it has the maximum number of nearest neighbors.

Connectivity: Bonded monomers can occupy either the same site (a repton or loop of stored length) or nearest neighbor sites (an extended bond).

Order: Ring monomers remain ordered even if several connected monomers occupy the same site [56].

Double-folding: Each extended bond of the polymer is paired with exactly one extended bond pointing in the opposite direction [Fig. 1(b)].

Ring monomers and tree nodes: The number of ring monomers belonging to the same tree node is equal to $f + \alpha$, where f is the functionality of the lattice tree node and α is the number of loops of stored length on that node.

Excluded volume interaction: Different tree nodes are not allowed to occupy the same lattice site.

Dynamics: We employ a simple Metropolis scheme [58] which consists of trying to move a randomly selected monomer to a randomly chosen site out of the twelve possible nearest neighbors. The move is only accepted if the new conformation respects the conformational rules above.

A two-dimensional (hexagonal) representation of a double-folded polymer chain conformation produced using the model is shown in Fig. 1(d). The green (red) color indicates the allowed (forbidden) moves according to the conformational

TABLE I. System parameters for the double-folded ideal rings (Ideal), double-folded self-avoiding rings (S.A.T), and double-folded rings in the melt state (Melt). N : Number of monomers per chain; n_p : Total number of chains per simulated system; L_{box} : Size of the simulation box. Note: An FCC lattice of size L contains $\frac{L^3}{2}$ sites; Site occupation number: The average number of monomers in an occupied lattice site; ρ : Lattice density which is the ratio of the number of occupied sites to the total number of sites; N_{sample} : Number of independent MC samples; T_{tot} : simulation run time in Monte Carlo sweep [MCs]; CPU time: The CPU wall clock time for N_{sample} samples on a single core; N_{ind} : The number of independent configurations (see Sec. IV C); τ_{max} : Configuration relaxation time measured after reaching equilibrium calculated using, $\tau_{\text{max}} = \frac{T_{\text{tot}}}{2N_{\text{ind}}}$. Radius of gyration $\langle R_g^2 \rangle$, MSID $\langle R^2(N/2) \rangle$, and average value of contour distance $\langle L(N) \rangle$ are defined in the text. All times are measured in Monte Carlo sweep [MCs], all distances are in units of lattice constants, and all measurements are performed after reaching equilibrium.

N	n_p	L_{box}	Site occupation	ρ	N_{sample} [$\times 10^2$]	T_{tot} [$\times 10^4$]	CPU time [days]	N_{ind} [$\times 10^4$]	τ_{max} [$\times 10^4$]	$\langle R_g^2 \rangle$	$\langle R^2(N/2) \rangle$	$\langle L(N) \rangle$
Ideal												
64	1	8	2.7(7)	$9.1(1) \times 10^{-2}$	16	10^3	~ 0.4	$\sim 10^2$	~ 0.8	2.13 ± 0.01	5.74 ± 0.13	4.38 ± 0.03
216	1	12	3.4(7)	$7.2(6) \times 10^{-2}$	16	10^4	~ 5	~ 38	~ 21	4.27 ± 0.03	11.13 ± 0.26	8.51 ± 0.06
512	1	16	3.9(8)	$6.3(4) \times 10^{-2}$	16	10^4	~ 16.5	~ 3.6	$\sim 2.2 \times 10^2$	7.13 ± 0.06	18.56 ± 0.44	13.59 ± 0.1
1000	1	20	4.3(2)	$5.8(6) \times 10^{-2}$	6.4	10^5	~ 74	~ 2.4	$\sim 1.3 \times 10^3$	10.52 ± 0.14	27.37 ± 1.02	19.18 ± 0.23
S.A.T												
64	1	20	2.3(6)	$6.7(8) \times 10^{-3}$	16	10^3	~ 0.2	~ 81	~ 0.9	3.53 ± 0.02	10.25 ± 0.21	4.84 ± 0.04
216	1	32	2.3(5)	$5.6(1) \times 10^{-3}$	16	10^4	~ 4.5	~ 27	~ 29	11.76 ± 0.08	34.61 ± 0.72	10.96 ± 0.09
512	1	80	2.3(4)	$8.5(5) \times 10^{-4}$	16	10^4	~ 17.5	~ 2.6	$\sim 3 \times 10^2$	28.65 ± 0.20	85.01 ± 1.78	19.77 ± 0.17
1000	1	100	2.3(5)	$8.5(2) \times 10^{-4}$	6.4	10^5	~ 30.7	~ 1.8	$\sim 1.7 \times 10^3$	55.95 ± 0.62	166.42 ± 5.55	30.64 ± 0.35
Melt												
64	12	8	3.1(5)	$9.5(3) \times 10^{-1}$	16	10^3	~ 4.5	$\sim 2 \times 10^3$	~ 0.4	2.08 ± 0.01	5.82 ± 0.03	3.63 ± 0.04
216	12	12	3.1(8)	$9.4(4) \times 10^{-1}$	8	10^4	~ 76	$\sim 3.4 \times 10^2$	~ 14.1	5.72 ± 0.01	15.99 ± 0.13	8.03 ± 0.06
512	12	16	3.1(8)	$9.4(4) \times 10^{-1}$	6.4	10^4	~ 165	~ 22	$\sim 1.6 \times 10^2$	11.33 ± 0.03	31.33 ± 0.30	13.69 ± 0.18
1000	12	20	3.1(8)	$9.4(3) \times 10^{-1}$	2.56	10^5	~ 749	~ 15	$\sim 9.7 \times 10^2$	18.89 ± 0.14	52.04 ± 1.15	20.46 ± 0.42

constraints. All allowed hopping moves for tightly folded rings can be classified in terms of two different move types:

The Repton move: A unit of stored length hops one unit along the tree without changing its structure [indicated with the green letter (R) in Fig. 1(d)].

The Hairpin move: If there is at least one connected loop of stored length (in a site) on each side of a monomer, both loops can unfold and result in an extended bond (creation). Naturally, the inverse move removes an extended bond pair and thus shortens or removes a side branch from the tree structure (annihilation). In fact, branched structures are introduced by the formation of hairpins [green letter (H) in Fig. 1(d)].

An example of a rejected move is also shown in Fig. 1(d). The red move (F) will lead to a forbidden conformation because it does not preserve the double-folded structure. For an impression of the dynamics of the appearance and disappearance of branches due to Hairpin moves, we refer the reader to the opening sequences of the Supplemental Material, video S4 [59].

C. Studied systems

The simulations were carried out for chain lengths varying between 64 to 1000 for three systems: ideal double-folded rings, self-avoiding double-folded rings, and rings in the melt state. The self-avoiding case and the rings in the melt state have excluded volume interactions. For the ideal case, there

is no restriction on the number of tree nodes on any site of the lattice (no excluded volume interaction). In the melt state a high lattice density, $\rho = 0.95$, was used. Since polymer chains diffuse very slowly in compact systems, we have performed long simulation runs to have a large number of independent samples. For the self-avoiding double-folded ring simulations the size of the box was set large enough to avoid self-interaction of the chain as a result of the periodic boundary condition. A summary of the simulation parameters and data is given in Table I.

D. Initialization and equilibration

Initial configurations are produced through a growth process. First, double-folded rings are seeded as trimers which are located on a common lattice site. Then the process comprises two operations:

(i) The diffusion of the monomers, in agreement with the previously stated dynamic rules. If branching is allowed during the growth process, highly branched compact chain configurations appear on the lattice. However, if branching is not allowed during growth, the Hairpin move is restricted to the chain ends. As a result, a double-folded ring configuration will be built which resembles a self-avoiding random walk in space.

(ii) The occasional addition of new monomers. A new monomer is introduced to a chain by selecting a random monomer on the chain and inserting the new one between the selected monomer and the next neighbor along the chain, on

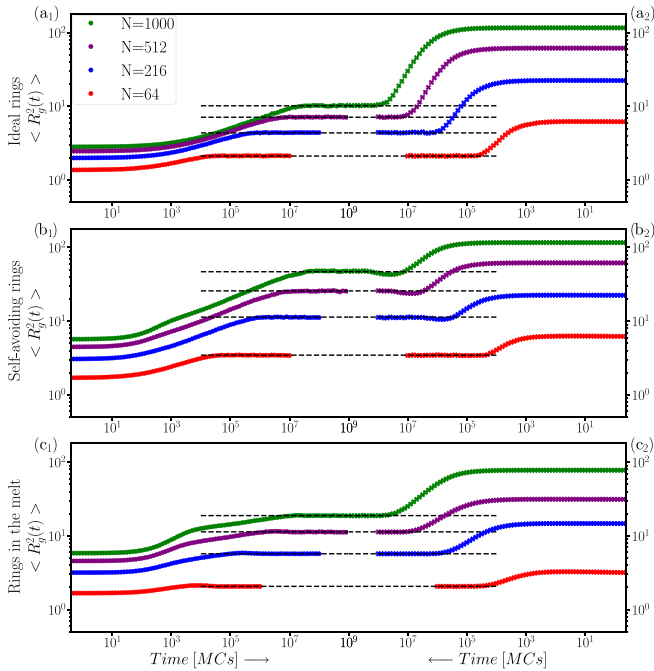


FIG. 2. Equilibration monitored using the mean-square radius of gyration as a function of time. Comparison between initially branched, compact double-folded chains (left column), and initially double-folded chains with no branches (right column) for three different systems: (a) ideal double-folded rings, (b) self-avoiding double-folded rings, and (c) double-folded rings in the melt state. The horizontal lines represent the average values after the chains have reached equilibrium. For better visualization, the time direction is reversed in the right column. In all three systems, at large times both initial states (from left and right) reach the same equilibrium values (reported in Table I).

the same site. In other words, we add a loop of stored length. The insertion of a loop is attempted with low probability, 0.01, to assure a good balance between growth and equilibration. The addition of new monomers is halted once all chains have the desired length. This process results in unknotted and non-concatenated rings.

The radius of gyration is the structural property that has been investigated to monitor the state of equilibration of the polymer systems. The mean-square gyration radius $\langle R_g^2 \rangle$ is the average squared distance of any point in the ring polymer chain from its center of mass. The systems have reached equilibrium when this quantity no longer changes. All reported quantities are taken from the simulation regime where the polymers are fully equilibrated.

Figure 2 shows the radius of gyration vs MC time (one MC sweep is equivalent to one MC trial for every monomer in the system) for different rings. In order to validate the equilibrium values of radius of gyration, we ran the simulations from two totally different initial conditions. The left column in Fig. 2 shows equilibration of compact initial configurations, which swell as the simulation progresses with time. The right column shows equilibration of more open, initially unbranched double-folded rings, where average ring size decreases as branches appear. The horizontal lines represent the average values after the chains have reached equilibrium (values are

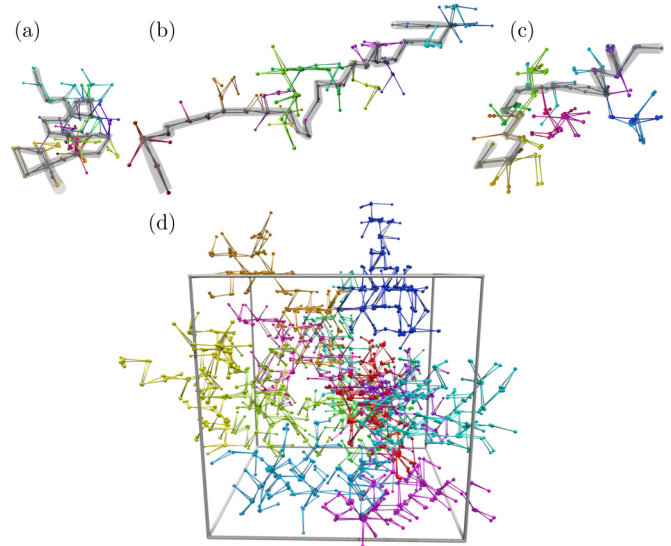


FIG. 3. Equilibrated simulation snapshots of (randomly selected) configurations of the double-folded rings with $N = 216$. Successive segments are represented with a HSV cyclic color map. (a) A single double-folded ideal ring; (b) a single double-folded self-avoiding ring; (c) a single double-folded ring in the melt state. The gray tubes show the longest paths of the trees. All the trees have the same bond scale. The size of the ring in the melt is larger than the ideal tree and smaller than the self-avoiding tree. (d) Sample configuration of the melt with 12 double-folded rings. Each ring is represented with a different color. The snapshots were produced using Blender 2.8 [60]. 3D views of these configurations are available in the Supplemental Materials, videos S1, S2, and S3 [59].

reported in Table I). In particular, Fig. 2 confirms that the simulation results do not depend on the initial conformations of the ring polymer chains.

IV. RESULTS AND DISCUSSIONS

After some first qualitative insights in Sec. IV A, we present a quantitative analysis of the conformational statistics and dynamics of our randomly branching, double-folded ring polymers and compare our observations to available exact results and predictions of the scaling theories presented in Secs. IV B and IV C. We close by comparing the dynamics of double-folded rings to the motion of linear chains in the tube model [47] (Sec. IV D).

A. Qualitative insights

Figure 3 illustrates configurations of our lattice model for double-folded ring polymers as they emerge from our simulations after the systems have reached equilibrium. Ring monomers are shown as small spheres which are displaced from their actual position by a small random offset. This representation reveals (i) multiple occupancy of lattice sites and (ii) Double-folding. Specifically, we show a sample configuration of (a) an ideal double-folded ring, (b) a self-avoiding double-folded ring, and (c) a double-folded ring in the melt state with 216 monomers, as well as (d) a view of a corresponding melt configuration (unfolded from the simulation box) for 12 double-folded rings. The gray tubes show the

longest paths along the trees. Three-dimensional (3D) views of these configurations are available in the Supplemental Material, videos S1, S2, and S3 [59]. For the ideal case there is no restriction on the number of monomers on each site. Rings in the melt state and, in particular, isolated self-avoiding rings appear swollen relative to the ideal case. At least qualitatively, this is the expected [36] consequence of excluded volume interactions and the partial screening in melts. In the self-avoiding case, the structure is quite anisotropic and the longest path is aligned along the longest axis. In the melt case, the structure is more compact and spherically symmetric, and the mass is almost equally distributed between the branches.

A sequence of snapshots of the time evolution of a (randomly selected) self-avoiding double-folded ring with $N = 216$ monomers at logarithmic time intervals (indicated on the top left) is available in the Supplemental Material, video S4 [59]. The gray tube shows the longest path along the tree at $T = 0$, where T is set to zero after reaching equilibrium. As a result of the local mass transport (both in space and along the tree), three distinct dynamical regimes can be observed. (i) At short timescales ($T \lesssim 10^2$ [MCs]), at the beginning of the video, the relaxation is dominated by the small intra-branch dynamics and the spontaneous formation and deletion of short side-branches in the tree structure. (ii) At intermediate timescales, longer side-branches appear and disappear but the core trunk remains stable. (iii) Near the end of the video ($T \gtrsim 10^6$ [MCs]), the entire tree diffuses in space.

Finally, the Supplemental Material video S5 [59] follows the motion of the same ring over even longer times to illustrate that its internal structure completely relaxes on timescales over which the ring diffuses over a distance corresponding to its own size.

B. Conformational statistics

To analyze the secondary and tertiary structure of our double-folded ring polymers as discussed in Secs. II A and II B, we have calculated the tree contour distance $L(i, j)$ and square spatial distance $R^2(i, j)$ between all pairs of ring monomers i and j .

The tree contour distance $L(i, j)$ is defined as the length of the shortest path on the tree connecting i and j . $L(i, j)$ only depends on the tree connectivity and is completely independent of the spatial embedding of the double-folded ring polymer (details in the Appendix). Conversely, the calculation of the spatial distance, $R^2(i, j)$, is straightforward given the monomer positions and completely independent of the secondary structure.

Nevertheless, $L(i, j)$ and $R^2(i, j)$ are closely related, since the configurational statistics of the shortest path between two monomers on the tree is expected to follow a typical power-law relation, $\langle R^2(L) \rangle \sim L^{2\nu_{\text{path}}}$, for linear chains [Eq. (5)]. For ideal chains, $\nu_{\text{path}} = 1/2$ so that $\langle R^2(L_{ij}) \rangle \sim L_{ij}$. Excluded volume interactions cause a characteristic swelling with $\nu_{\text{path}} > 1/2$. To allow for a direct comparison, the various panels in Figs. 4–7 with our results for the secondary and tertiary structure always show corresponding data for these two quantities side by side.

Results for averaging $L(n)$ and $R^2(n)$ for the three systems under investigation over monomer pairs with identical ring

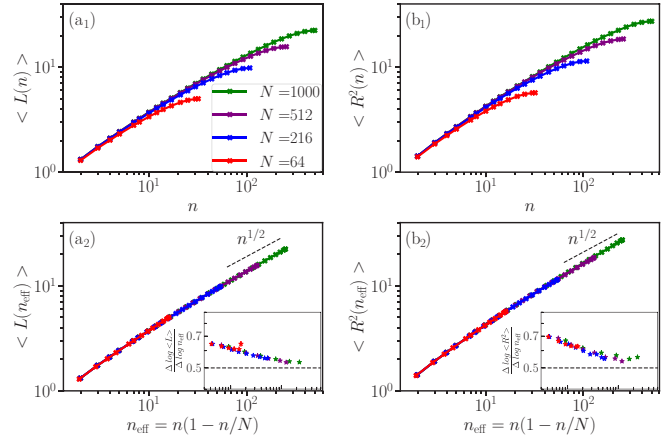


FIG. 4. Conformational statistics of ideal double-folded rings for four different chain lengths (described in the legend). Data are shown for ring contour distances up to $N/2$. Column (a) are the average values of the tree contour distances between all possible pairs of monomers, $\langle L(n) \rangle \sim n^\rho$. Column (b) plots the squared internal distances as a function of n , $\langle R(n)^2 \rangle \sim n^{2\nu}$. The exact exponents for the ideal case are $\rho = 1/2$ and $\nu = 1/4$. In panels (a₂) and (b₂) data are plotted as a function of n_{eff} , which effectively reduces finite size effects. The straight dashed lines correspond to the expectation scaling exponents. (a₂) and (b₂) insets show the local slopes of the data in panels (a₂) and (b₂), respectively. These effective exponents appear to converge to the theoretical exponents (dashed horizontal lines). Error bars are the same size or smaller than the symbols.

contour distance, $n = |i - j|$, are shown in panels (a₁) and (b₁) of Figs. 4–6. As expected, the results are ring size independent at small scales and reach a plateau on approaching the maximal ring contour distance of $n = N/2$.

Panels (a₂) and (b₂) in Figs. 4–6 show the same data plotted as a function of an effective ring contour distance, $n_{\text{eff}} = n(1 - n/N)$, introduced in Sec. II B. This representation reduces the finite ring size effects sufficiently for a

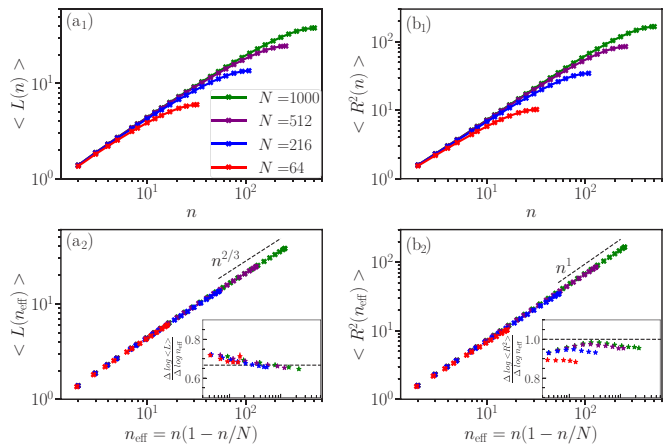


FIG. 5. Conformational statistics of self-avoiding double-folded rings. Column (a) plots the average value of the tree contour distances between all possible pairs of monomers. Flory theory predicts $\langle L(n) \rangle \sim n^{2/3}$. Column (b) plots the squared internal distance as a function of n . The exact scaling exponent is $\langle R(n)^2 \rangle \sim n^1$. Notation and symbols are as in Fig. 4.

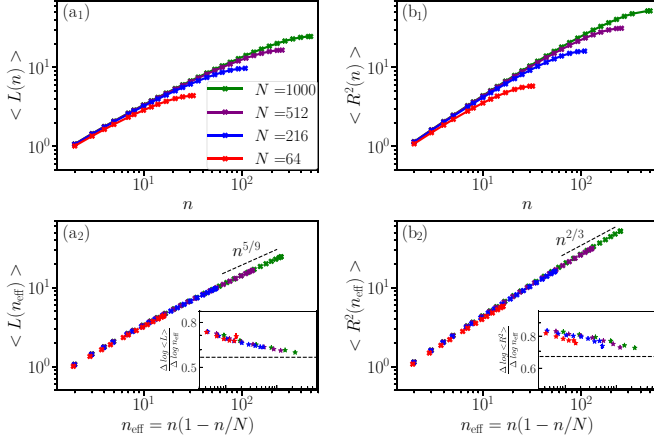


FIG. 6. Conformational statistics of double-folded annealed trees in the melt state. Column (a) plots the average value of the tree contour distances between all possible pairs of monomers. Flory theory predicts, $\langle L(n) \rangle \sim n^{5/9}$. Column (b) plots the squared internal distance as a function of n . Flory theory predicts, $\langle R(n)^2 \rangle \sim n^{2/3}$. Notations and symbols are as in Fig. 4.

meaningful comparison with the expected power law relations $\langle L(n) \rangle \sim n^\rho$ and $\langle R^2(n) \rangle \sim n^{2\nu}$. The dashed lines have slopes corresponding to the exact value or the predictions of Flory theory for these exponents in the asymptotic limit of infinite ring size. In addition, we have extracted effective exponents by calculating the derivatives using the logarithm of neigh-

boring data points, $(\frac{\Delta \log \langle L(n_{\text{eff}}) \rangle}{\Delta \log n_{\text{eff}}})$ and $(\frac{\Delta \log \langle R^2(n_{\text{eff}}) \rangle}{\Delta \log n_{\text{eff}}})$. Our results are shown in the inset of panels (a₂) and (b₂) of Figs. 4–6. The horizontal lines show again the expected exponents in the asymptotic limit of infinite ring size.

As a complement, we have analyzed the average tree contour distance $\langle L(N) \rangle$ and the mean-square gyration radius $\langle R_g^2(N) \rangle$ as a function of the chain length (Fig. 7), where the averages of the tree contour and spatial distances is calculated over all monomer pairs irrespective of their distance along the ring. A summary of these values for the studied systems is provided in Table I. Again, we have calculated the local exponents based on the slopes of the data points. The results are shown in the inset of panels of Fig. 7.

Like in comparable simulations of lattice trees [33,34], none of our systems has truly reached the asymptotic regime. Nevertheless, the observed values and trends (which represent crossovers between numerous regimes for linear or branched structures without or with full or partially screened excluded volume interactions [36]) are in good agreement with the theoretical expectations.

C. Dynamics

Having obtained a brief characterization of conformational and structural properties of the double-folded rings, we can now turn our attention to their dynamics. Polymer dynamics is usually analyzed by monitoring the mean-square displacements (MSD) of individual monomers and of the chain centers of mass (CM) with time (as mentioned in Sec. IID). Figures 8–10 show our results for

- (i) The total monomer mean-square displacement,

$$g_1(t) = \langle |\mathbf{r}_i(t) - \mathbf{r}_i(0)|^2 \rangle,$$

- (ii) The monomer mean-square displacement relative to the chain's center of mass,

$$g_2(t) = \langle |\mathbf{r}_i(t) - \mathbf{r}_i(0) - \mathbf{r}_{CM}(t) + \mathbf{r}_{CM}(0)|^2 \rangle,$$

- (iii) The mean-square displacement of the chain center of mass,

$$g_3(t) = \langle |\mathbf{r}_{CM}(t) - \mathbf{r}_{CM}(0)|^2 \rangle,$$

for single ideal and self-avoiding double-folded ring polymers as well as for double-folded ring polymers in the melt state.

Panels (a) in Figs. 8–10 shows a comparison of $g_1(t)$, $g_2(t)$, and $g_3(t)$ for one chain length ($N = 216$). In all three systems we see that $g_1(t)$ is dominated by $g_2(t)$ at early MC times and by $g_3(t)$ at large times. Up to $\tau_0 \approx 10$ MC sweeps (MCs) the monomer and CM motion follow a trivial diffusive dynamics. The characteristic dynamics of double-folded rings discussed in Sec. IID sets in beyond τ_0 and extends up to a maximal time τ_{max} , where the internal monomer motion reaches a plateau, $g_2(t) = 2\langle R_g^2 \rangle$, while $g_3(t)$ crosses over to free diffusion.

Panels (b) and (c) in Figs. 8–10 show data for the monomer motion $g_2(t)$ and $g_1(t)$ for different chain lengths, N . In all cases, the monomer MSD in the early and the tree regime are independent of N before crossing over to a ring-size-dependent free diffusion regime. In particular, the data in the tree regime follow an effective power law close to the prediction $t^{\frac{2\nu}{\nu+2}}$ [Eq. (17)], indicated by dashed lines. The

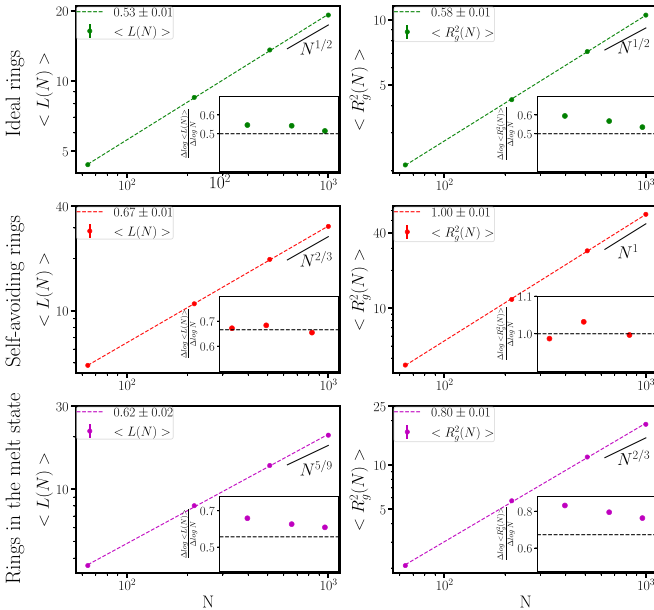


FIG. 7. Conformational statistics of double-folded rings. Left column: average tree contour distance $\langle L \rangle$ as a function of the chain length N . Straight lines correspond to the large- N behavior, $\langle L(N) \rangle \sim N^\rho$. Right column: ring mean-square gyration radius $\langle R_g^2 \rangle$ as a function of the chain length. Straight lines correspond to the large- N behavior, $\langle R(N)^2 \rangle \sim N^{2\nu}$. Insets show the local slopes of the data. These effective exponents appear to converge to the theoretical exponents (dashed horizontal lines). Error bars are the same size or smaller than the symbols.

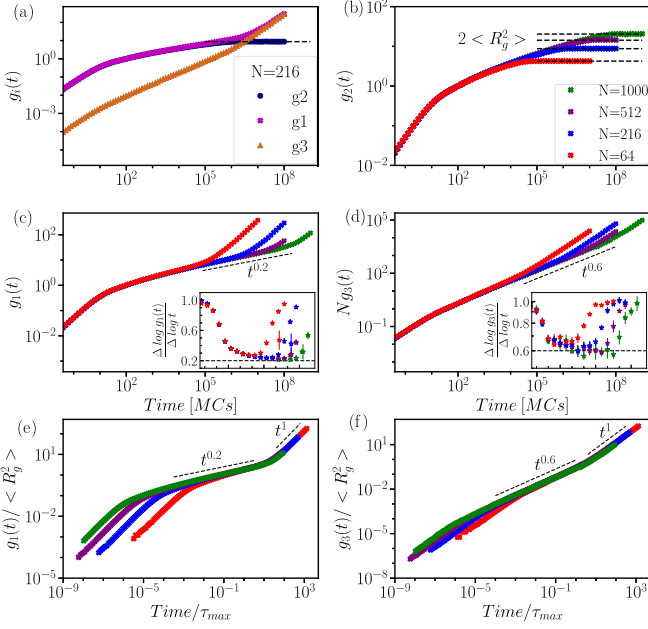


FIG. 8. MSDs for ideal double-folded rings. Panel (a) shows g_1 , g_2 , and g_3 for the ring with 216 monomers. The horizontal line corresponds to $2 \times \langle R_g^2 \rangle$. Panels (b), (c), and (d) plot $g_2(t)$, $g_1(t)$, and $N \times g_3(t)$ vs time in the unit of MCs, respectively. In panel (b) the horizontal lines correspond to $2 \times \langle R_g^2 \rangle$. In panels (c) and (d) the dashed lines have slopes corresponding to the prediction of the theory, $g_1(t) \sim t^{\frac{2\nu}{\nu+2}}$ and $g_3(t) \sim t^{\frac{2\nu+1}{\nu+2}}$. (c, d) Insets show the local slopes of the data. The effective exponents appear to converge to the theoretical exponents (dashed horizontal lines). Panels (e) and (f) show rescaled $g_1(t)$ and $g_3(t)$ with the mean-square gyration radii vs the rescaled time with the diffusion relaxation times.

crossovers between the three regimes are nicely revealed by the effective exponents, $(\frac{\Delta \log(g_i(t))}{\Delta \log t})$, shown in the insets of panels (c). While there are finite ring size effects, they essentially concern the width of the tree regime. The agreement with the expected exponents in the tree regime is excellent.

Panels (d) in Figs. 8–10 show the rescaled dynamics of the center of mass $g_3(t)$, multiplied by the ring size N , to compensate for the expected ring size dependence in the early and in the tree regime, Eq. (18). In both regimes data for different rings sizes collapse indeed on a universal scaling curve. In the tree regime, the data follow an effective power law close to the prediction $t^{\frac{2\nu+1}{\nu+2}}$ [Eq. (18)], indicated by dashed lines. Again, the various regimes can be clearly identified when considering the effective exponents, $(\frac{\Delta \log(g_3(t))}{\Delta \log t})$, shown in the insets of panels (c). Interestingly, the effective exponent for the dynamics of self-avoiding double-folded rings initially drops close to the value expected in the ideal case before increasing to a value in good agreement with the theoretical prediction.

Panels (e) and (f) in Figs. 8–10 explore the crossover of the monomer and the CM MSD from the tree to the free diffusion regime. For this purpose we rescale $g_1(t)$ and $g_3(t)$ with the mean-square gyration radii, $\langle R_g^2(N) \rangle$, of the corresponding rings. To rescale the time axis, we empirically defined a “diffusion relaxation time” as the time when the mean-square

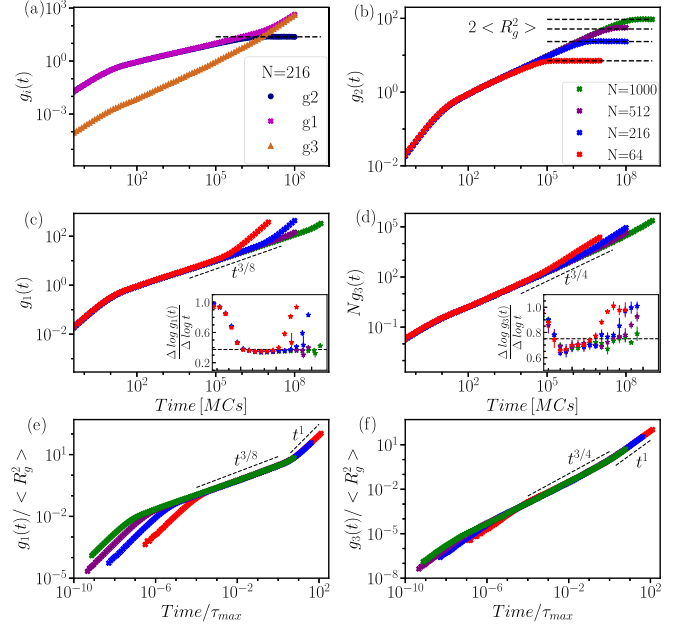


FIG. 9. MSDs for self-avoiding double-folded rings. Notation and symbols are as in Fig. 8.

displacement of the center of mass has moved a distance equal to the radius of gyration, $g_3(\tau_{\max}) = \langle R_g^2 \rangle$. The operation leads to a perfect data collapse for all but the earliest times before the rings enter the tree regime.

The scaling theory predicts that the maximal relaxation time should vary as $\tau_{\max} \sim N^{2+\rho}$ with the ring size, Eq. (13). Besides the “diffusion relaxation time” defined above, we have also tested this relation for the correlation time of the mean-square gyration radius, $\langle R_g^2(N) \rangle$, which characterizes the tertiary structure of our double-folded rings. We have

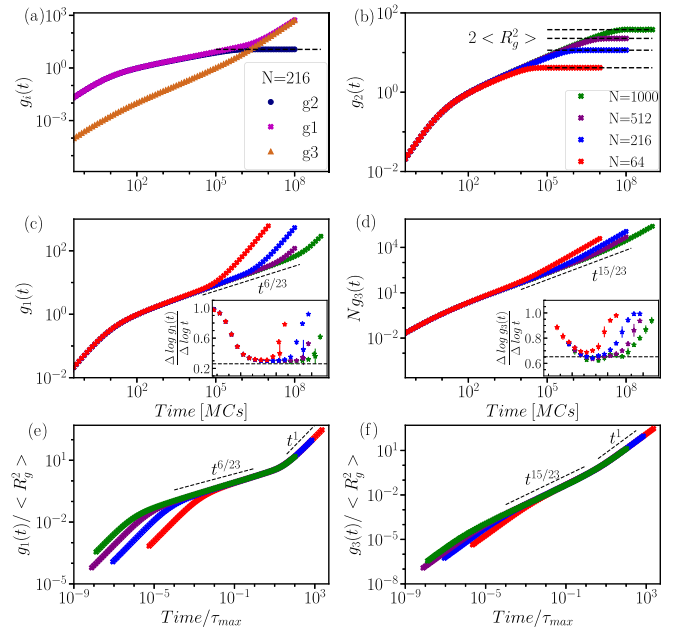


FIG. 10. MSDs for double-folded rings in the melt state. Notation and symbols are as in Fig. 8.

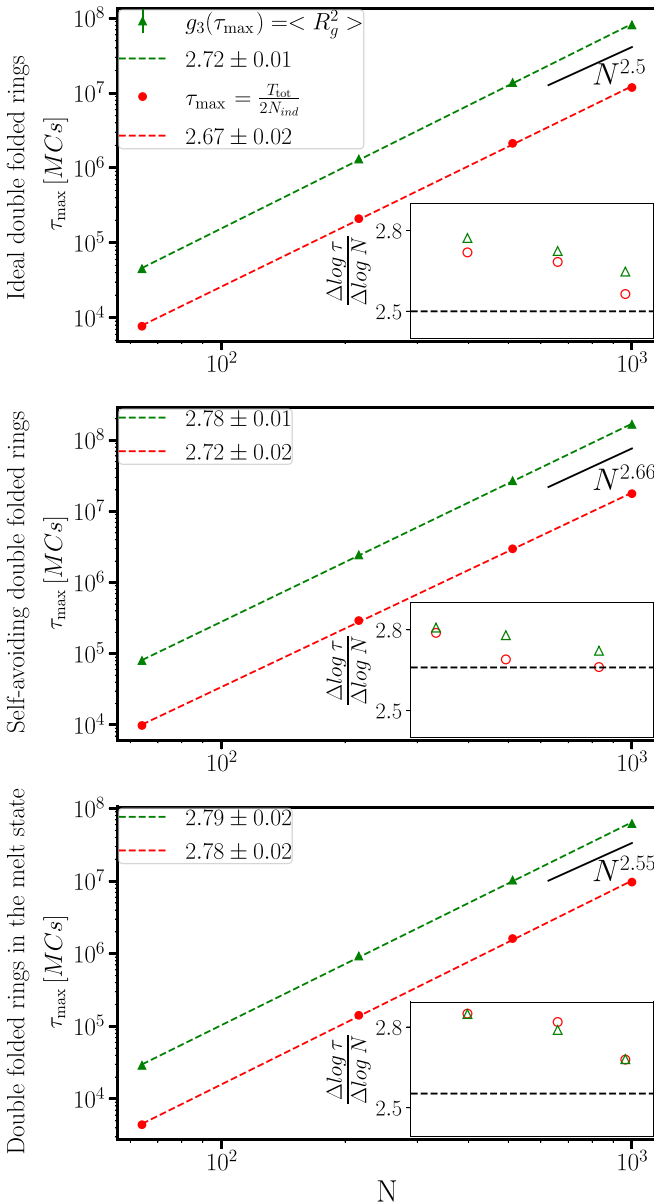


FIG. 11. Relaxation time in units of MCs vs N (chain length). Diffusion relaxation time (triangles) is calculated where $g_3(\tau_{\max})$ and $\langle R_g^2 \rangle$ are equal. Configurational relaxation time (circles) is calculated using $\tau_{\max} = \frac{T_{\text{tot}}}{2N_{\text{ind}}}$, where N_{ind} is number of independent samples. The black solid lines indicate the theoretically predicted slopes, $\tau_{\max} \sim N^{2+\rho}$, while the dashed lines are the best fit. Insets show the local slopes of the data. These effective exponents appear to converge to the theoretical exponents (dashed horizontal lines).

inferred this configurational relaxation time via the equation $\tau_{\max} = \frac{T_{\text{tot}}}{2N_{\text{ind}}}$ [61] from the number, N_{ind} , of independent samples we have obtained for the observable as estimated from a block averaging procedure [62]. Our results for the three investigated classes of double-folded ring polymers are plotted in Fig. 11. In all three cases, the configurational relaxation times are smaller than the diffusion relaxation times, but both estimates of τ_{\max} scale in the same way. The corresponding effective exponents shown in the inset are somewhat larger than expected. While our values are compatible with an

approach to the asymptotically expected exponent, a quantitative analysis probably requires data for larger systems.

D. Dynamics of double-folded rings vs linear chains

As summarized in Sec. IV C, the scaling theory [3,4,8] of the dynamics of randomly branching double-folded ring polymers focuses on the mass transport along the longest linear path on the tree. Given the similarities to the tube model for linear chains [e.g., Eq. (13) for the maximal relaxation time, $\tau_{\max}(N) \sim N^{\rho+2}$, applies in both cases], one could be tempted to think of the ring motion as a generalized form of reptation along their longest paths.

To test this analogy, we have visualized the equilibrium dynamics of the longest path of a randomly selected self-avoiding double-folded ring (Supplemental Material, video S6 [59]) and of a randomly selected double-folded ring in the melt state (Supplemental Material, video S7 [59]). Note that in these movies time progresses exponentially to cover the large gap between the timescales relevant to motion on the monomer and on the ring scale, respectively. Furthermore, we show fading images of previous conformations to simplify comparisons with the current conformation.

At early times, the behavior is very similar to contour length fluctuations for linear chains in the tube model: the bulk of the longest path remains unchanged, while the path ends fluctuate. But after a while much more drastic changes appear, where the longest path appears to jump in space. For a linear chain such a jump of the primitive chain would necessarily require a corresponding transport of mass. For our rings the movie insets show that the jumps in the position of the longest path are not accompanied by major changes in the ring configurations. Instead, the jumps are due to the continuous redistribution of mass between the side branches, which at some point cause a substantially different path to outgrow the original longest path.

There are qualitative differences between the two types of ring systems. In the self-avoiding case, during relaxation, short side branches relax first. This manifests itself at the ends of the backbone whose center portion remains unchanged. At later times, longer side branches relax and randomly one or two side branches start to grow. Beyond the relaxation time the backbone changes as a whole as a result of modified branching. In the melt case, the structure is more compact and spherically symmetric. The mass is almost equally distributed between the branches. Hence, a small change in the side branches may immediately lead to a completely new path for the longest backbone. This can be observed by comparing videos S6 and S7 [59]. A quantitative study [35] pursued the statistics of the branch weight distributions in the melt state, but a study of the dynamics of the distribution of side branches is still required.

Since it is not possible to follow the temporal evolution of a particular path on an internally rearranging tree, it is easier to focus on pairs of monomers (i^* , j^*), which at some time, $t = 0$, are located on opposite ends of the longest path on the primitive tree. Typically these monomers are also relatively remote along the ring contour, their contour distances following a broad distribution of around $|i^* - j^*| = N/2$. In the movie insets we used bigger spheres to mark two such pairs of

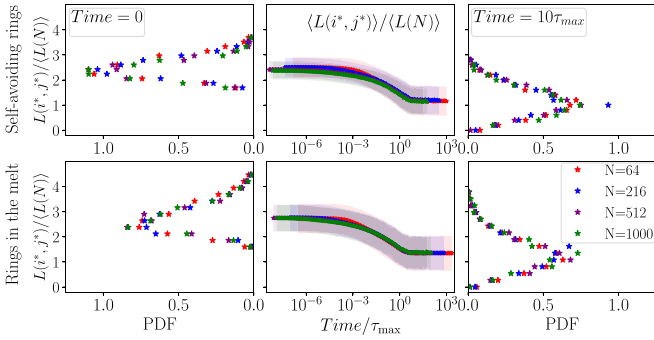


FIG. 12. Tree contour distances between monomers (i^* , j^*) flanking the longest path on the tree at an arbitrarily chosen time $t = 0$ after equilibration. Left-hand side column: Rescaled probability distributions of the longest path length, $L_{\max} = L(i^*, j^*, t = 0)$. Middle column: Rescaled time evolution of $\langle L(i^*, j^*, t) \rangle$. Right-hand side column: Rescaled probability distributions of the tree contour distance, $L(i^*, j^*, t = 10\tau_{\max})$, between (i^* , j^*) after all memory of the initial state at $t = 0$ is lost. Top row: Self-avoiding double-folded rings. Bottom row: Double-folded rings in the melt state.

monomers which flank the longest path at the beginning and the end of the visualized sequences.

Figure 12 presents a quantitative analysis of the tree contour distance $L(i^*, j^*, t)$ between these monomers rescaled by the average tree contour distance $\langle L(N) \rangle$ reported in Table I. The panels on the left-hand side shows the distribution of the tree contour distances at $t = 0$, i.e., for $L(i^*, j^*, t = 0) \equiv L_{\max}(t = 0)$. Results for different ring sizes superpose, indicating that both the average and width of the distribution scale with $\langle L(N) \rangle \sim N^\rho$. In contrast, for linear chains contour length fluctuations, $\sqrt{\langle \delta L_{pp}^2 \rangle} \sim \sqrt{N}$, become asymptotically negligible compared to the average length, $\langle L_{pp} \rangle \sim N$, of the primitive paths [31]. The central panels in Fig. 12 show the decay of $\langle L(i^*, j^*, t) \rangle$ from a value of $(2.44 \pm 0.03$ to $1.15 \pm 0.01) \times \langle L(N) \rangle$ for self-avoiding rings and $(2.77 \pm 0.01$ to $1.33 \pm 0.01) \times \langle L(N) \rangle$ for rings in the melt over a timescale of the order of the “diffusion relaxation time,” τ_{\max} . Again, the suitably rescaled data for different ring sizes exhibit a reasonable collapse. The true extent of the (tree) “contour length fluctuations” is better represented by the distribution functions of $L(i^*, j^*, t = 10\tau_{\max})$ shown in the panels on the right-hand side of Fig. 12. While the monomers (i^* , j^*) located at opposite ends of the longest path on the tree at $t = 0$ have a finite chance to form secondary structure contacts [50] with $L(i^*, j^*, t) \equiv 0$ at later times, a corresponding deep retraction of one end of a linear chain to the opposite end of the tube is exponentially rare [31].

We conclude that randomly branching double-folded ring polymers move quite differently from reptating linear chains. In particular, the dynamics of rings of all sizes is dominated by the analog of contour length fluctuations occurring simultaneously between all pairs of monomers of the rings.

V. SUMMARY AND CONCLUSION

Supercoiled DNA, crumpled interphase chromosomes, and topologically constrained ring polymers often adopt treelike, double-folded, randomly branching configurations.

To explore the statistical and dynamical properties of such objects, we have performed Monte Carlo simulations of a suitable elastic lattice polymer model which accounts for double folding [4,43], the local accumulation of contour length on the primitive tree [4,40,44–46], as well as excluded volume interactions [44–46]. In particular, we have studied single ideal double-folded rings, single self-avoiding double-folded rings, and double-folded rings in the melt state.

In our simulations, side branches of the primitive tree characterizing the double-folded rings are spontaneously created and deleted as a consequence of the local monomer motion. Since the diffusive mass transport is local both in space and on the connectivity graph of the tree, we expect our systems to fall into the same universality class as the experimental target systems.

The observed static properties are in good agreement with exact results and predictions of Flory theory for randomly branching polymers. For example, in the melt state rings adopt compact configurations and exhibit territorial behavior. In particular, the model reproduces results from previous simulations of double-folded ring polymers [50], which were wrapped *a posteriori* around randomly branching polymers generated in corresponding simulations on the tree level [33–35] in an attempt to devise a numerically efficient multiscale approach to the simulation of nonconcatenated ring polymer melts and interphase nuclei [11,12].

The present approach offers the advantage that the dynamics of the ring degrees of freedom can be followed together with the evolution of the tree structure. This is a key feature for the simulation of copolymer [63] models of crumpled [14,15] or supercoiled [17,19,20] interphase chromosomes. Here we have used this information to show that the diffusion of the monomers and the rings’ center of mass are in excellent agreement with the predictions of a recent scaling theory [8]. Furthermore, we have explored a possible analogy between the motion of randomly branching double-folded ring polymers and reptating linear chains. While there exist formal similarities on the scaling level, we conclude that the dynamics of rings is rather dominated by the analog of contour length fluctuations, which constantly modify the distances between all monomers on the tree over a wide range.

ACKNOWLEDGMENTS

This work was only possible by generous grants of computer time by the PSMN computer center of the ENS-Lyon. We thank Angelo Rosa and Ivan Junier for valuable discussions and Ali Farnudi for his technical support. The authors would like to acknowledge the networking support by the “European Topology Interdisciplinary Action” (EUTOPIA) CA17139. R.E. acknowledges support by the National Science Foundation under Grant No. NSF PHY-1748958.

APPENDIX: CALCULATING TREE CONTOUR DISTANCES FOR TIGHTLY DOUBLE-FOLDED RINGS

1. Bridge bonds and tree contour distances

An example of a tree is illustrated in Fig. 13(a). The tree connectivity can be mapped on a circle as in Fig. 13(b), where consecutive monomers are represented with numbers. The

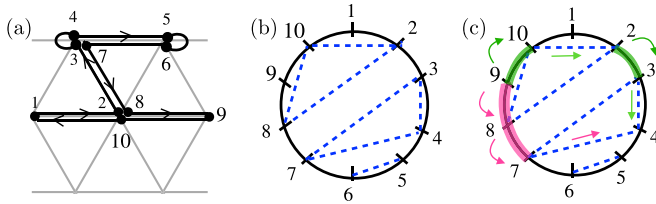


FIG. 13. (a) An example of a tree with side branches. (b) Ring connectivity of the example tree (a) mapped on a circle together with bridge bonds (dashed lines) that are formed during the “burning” process. (c) Illustration of the distance between monomers 9 and 4 following the bridge bonds along the way (green: clockwise, and pink: counterclockwise).

tree contour distance between two monomers of a double-folded ring can be calculated by following the ring contour while ignoring all the double-folded side branches along the way. Bridge bonds (represented with dashed lines) between monomers on each tree site can be defined to mark the location of possible side branches. The tree contour distance between any pair of monomers can be calculated by counting the number of steps taken on the circle and using the bridge bonds as shortcuts (shortcuts do not add to the number of steps). Obviously, the choice of direction (clockwise or counterclockwise) should result in the same contour length. For example, the tree contour distance between monomers 9 and 4 in Fig. 13(c) is 2.

2. Bridge bonds from spatial colocalization

In systems with excluded volume interactions, the identification of the bridge bonds is straightforward as they simply connect monomers which are colocalized in space (Fig. 13). However, as illustrated in Fig. 14, this method fails in the ideal case, where incorrectly identified extra bridges [red dashed line in Fig. 14(b)] lead to lattice animal-like connectivity graphs containing falsely identified loops.

3. Bridge bonds from an analysis of the local connectivity

We used a “pinching” variant of the “burning” algorithm [25,33,64] that takes advantage of the local connectivity information. As the algorithm operates by iteratively removing (pinching off) branch tips, it avoids the false identification of loops. The protocol to find the bridges layer by layer is as follows:

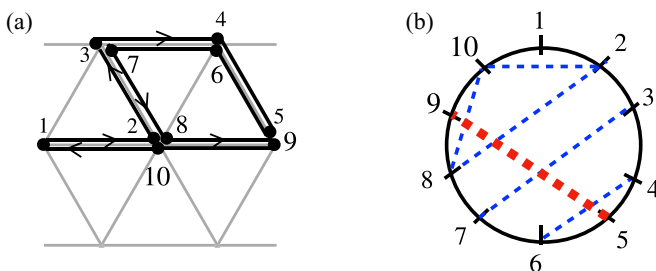


FIG. 14. (a) An example of the ideal double-folded ring. (b) Corresponding bridges. If all monomers on a site have bridges defined between them, it leads to an extra wrong bridge (red dashed line).

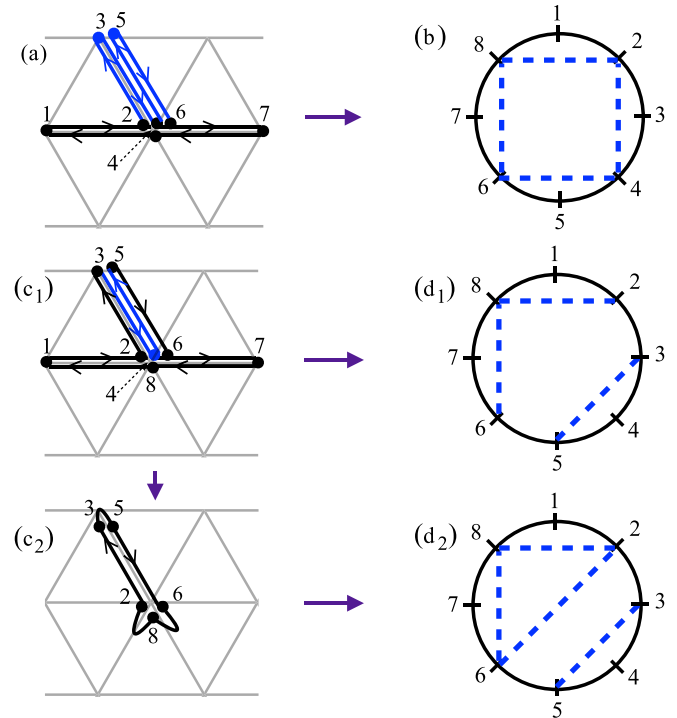


FIG. 15. An example of branch tip detection in an ideal double-folded ring. (a) and (c₁): Examples of side branches in the ideal case. Ambiguous branch tips and their corresponding bonds are shown in blue. The tree structure is the same, but different interpretations of branch tips are possible. (b) Bridge bonds corresponding to interpretation (a). Removal of the first layer of tips in (c₁) results in the formation of bridge bonds (d₁) and the tree structure (c₂). The removal of the second layer results in the completion of the bridge bond detection displayed in (d₂).

(A) Make a list of all the tree branch tips. A branch tip is defined as a monomer with attached bonds pointing in opposite directions, ignoring neighbor loops (with zero-length bonds). For example, in Fig. 13(a) monomers 1, 9, and 6 (5 is a loop) are branch tips.

(B) Randomly select a branch tip and remove it from the ring. For example, if the branch tip 9 is randomly selected, monomer 9 is removed and a bridge is defined between monomers 8 and 10.

(C) Repeat steps (A) and (B) until the branch tip list is exhausted.

(D) Steps (A)–(C) result in the removal of one “layer” of side branches. Repeat these steps (remove layer by layer) until all the branch tips are removed and all the bridge bonds are found.

We verified that the pinching algorithm reproduces the results from the spatial colocalization for double-folded rings with excluded volume interactions.

4. Ambiguities in the tree structure for ideal double-folded rings

The tree connectivity is not uniquely defined for the ideal double-folded rings. There is an intrinsic ambiguity in how side branches and the underlying tree structure is defined. An example is given in Figs. 15(a) and 15(c₁), where branch tips

under consideration and their attached bonds are colored blue. They both have the same tree structure, but the number of branch tips is open for interpretation:

(1) Figure 15(a): Branch tips are 1, 3 (pointing up), 5 (pointing up), and 7. During the burning of the first layer, all the branch tips are removed, which results in the bridging bonds shown in Fig. 15(b).

(2) Figure 15(c1): Branch tips are 1, 7, and 4 (pointing down from the tree node {3, 5}). Figure 15(d1) shows the

bridges corresponding to the burning of the first layer. In the next layer of burning, Fig. 15(c2), the bridge between monomers 2 and 6 is formed, Fig. 15(d2).

(1) and (2) are random outcomes of step (B) that result in different bridging bonds and therefore different tree contour lengths, as shown in Figs. 15(b) and 15(d2). In practice, we repeat the described procedure multiple times and consider the shortest tree contour distances among different interpretations.

-
- [1] A. Khokhlov and S. Nechaev, Polymer chain in an array of obstacles, *Phys. Lett. A* **112**, 156 (1985).
- [2] M. Cates and J. Deutsch, Conjectures on the statistics of ring polymers, *J. Phys.* **47**, 2121 (1986).
- [3] M. Rubinstein, Dynamics of Ring Polymers in the Presence of Fixed Obstacles, *Phys. Rev. Lett.* **57**, 3023 (1986).
- [4] S. P. Obukhov, M. Rubinstein, and T. Duke, Dynamics of a Ring Polymer in a Gel, *Phys. Rev. Lett.* **73**, 1263 (1994).
- [5] J. D. Halverson, W. B. Lee, G. S. Grest, A. Y. Grosberg, and K. Kremer, Molecular dynamics simulation study of nonconcatenated ring polymers in a melt. I. Statics, *J. Chem. Phys.* **134**, 204904 (2011).
- [6] M. Lang, Ring conformations in bidisperse blends of ring polymers, *Macromolecules* **46**, 1158 (2013).
- [7] A. Y. Grosberg, Annealed lattice animal model and Flory theory for the melt of non-concatenated rings: Towards the physics of crumpling, *Soft Matter* **10**, 560 (2014).
- [8] J. Smrek and A. Y. Grosberg, Understanding the dynamics of rings in the melt in terms of the annealed tree model, *J. Phys.: Condens. Matter* **27**, 064117 (2015).
- [9] T. Ge, S. Panyukov, and M. Rubinstein, Self-similar conformations and dynamics in entangled melts and solutions of nonconcatenated ring polymers, *Macromolecules* **49**, 708 (2016).
- [10] J. Smrek and A. Y. Grosberg, Minimal surfaces on unconcatenated polymer rings in melt, *ACS Macro Lett.* **5**, 750 (2016).
- [11] A. Rosa and R. Everaers, Ring Polymers in the Melt State: The Physics of Crumpling, *Phys. Rev. Lett.* **112**, 118302 (2014).
- [12] R. D. Schram, A. Rosa, and R. Everaers, Local loop opening in untangled ring polymer melts: A detailed Feynman test of models for the large scale structure, *Soft Matter* **15**, 2418 (2019).
- [13] A. M. Gutin, A. Y. Grosberg, and E. I. Shakhnovich, Polymers with annealed and quenched branchings belong to different universality classes, *Macromolecules* **26**, 1293 (1993).
- [14] A. Rosa and R. Everaers, Structure and dynamics of interphase chromosomes, *PLoS Comput. Biol.* **4**, e1000153 (2008).
- [15] E. Lieberman-Aiden, N. L. van Berkum, L. Williams, M. Imakaev, T. Ragozcy, A. Telling, I. Amit, B. R. Lajoie, P. J. Sabo, M. O. Dorschner, R. Sandstrom, B. Bernstein, M. A. Bender, M. Groudine, A. Gnirke, J. Stamatoyannopoulos, L. A. Mirny, E. S. Lander, and J. Dekker, Comprehensive mapping of long-range interactions reveals folding principles of the human genome, *Science* **326**, 289 (2009).
- [16] J. F. Marko and E. D. Siggia, Statistical mechanics of supercoiled DNA, *Phys. Rev. E* **52**, 2912 (1995).
- [17] C. J. Dorman, DNA supercoiling and bacterial gene expression, *Sci. Prog.* **89**, 151 (2006).
- [18] J. Mondal, B. P. Bratton, Y. Li, A. Yethiraj, and J. C. Weisshaar, Entropy-based mechanism of ribosome-nucleoid segregation in E.coli cells, *Biophys. J.* **100**, 2605 (2011).
- [19] T. Lepage, F. Képès, and I. Junier, Thermodynamics of long supercoiled molecules: Insights from highly efficient Monte Carlo simulations, *Biophys. J.* **109**, 135 (2015).
- [20] T. Lepage and I. Junier, A polymer model of bacterial supercoiled DNA including structural transitions of the double helix, *Physica A* **527**, 121196 (2019).
- [21] L. Liu and C. Hyeon, Contact statistics highlight distinct organizing principles of proteins and RNA, *Biophys. J.* **110**, 2320 (2016).
- [22] J. Kelly, A. Y. Grosberg, and R. Bruinsma, Sequence dependence of viral RNA encapsidation, *J. Phys. Chem. B* **120**, 6038 (2016).
- [23] S. W. Singaram, A. Gopal, and A. Ben-Shaul, A Prüfer-sequence based algorithm for calculating the size of ideal randomly branched polymers, *J. Phys. Chem. B* **120**, 6231 (2016).
- [24] M. Rubinstein and R. Colby, *Polymer Physics* (Oxford University Press, Oxford, 2003).
- [25] A. Aharony and D. Stauffer, *Introduction to Percolation Theory* (Taylor & Francis, London, 2003).
- [26] G. Parisi and N. Sourlas, Critical Behavior of Branched Polymers and the Lee-Yang Edge Singularity, *Phys. Rev. Lett.* **46**, 871 (1981).
- [27] M. E. Fisher, Yang-Lee Edge Singularity and ϕ^3 Field Theory, *Phys. Rev. Lett.* **40**, 1610 (1978).
- [28] D. A. Kurtze and M. E. Fisher, Yang-Lee edge singularities at high temperatures, *Phys. Rev. B* **20**, 2785 (1979).
- [29] J. F. A. Bovier and U. Glaus, Branched polymers and dimensional reduction, in *Critical Phenomena, Random Systems, Gauge Theories*, edited by K. Osterwalder and R. Stora (North-Holland, Amsterdam, 1884).
- [30] P.-G. De Gennes, *Scaling Concepts in Polymer Physics* (Cornell University Press, Ithaca, New York, 1979).
- [31] M. Doi and S. F. Edwards, *The Theory of Polymer Dynamics* (Oxford University Press, New York, 1986).
- [32] A. Y. Grosberg and A. R. Khokhlov, *Statistical Physics of Macromolecules* (AIP Press, New York, 1994).
- [33] A. Rosa and R. Everaers, Computer simulations of randomly branching polymers: Annealed versus quenched branching structures, *J. Phys. A: Math. Theor.* **49**, 345001 (2016).
- [34] A. Rosa and R. Everaers, Computer simulations of melts of randomly branching polymers, *J. Chem. Phys.* **145**, 164906 (2016).

- [35] A. Rosa and R. Everaers, Beyond Flory theory: Distribution functions for interacting lattice trees, *Phys. Rev. E* **95**, 012117 (2017).
- [36] R. Everaers, A. Y. Grosberg, M. Rubinstein, and A. Rosa, Flory theory of randomly branched polymers, *Soft Matter* **13**, 1223 (2017).
- [37] W. A. Seitz and D. J. Klein, Excluded volume effects for branched polymers: Monte Carlo results, *J. Chem. Phys.* **75**, 5190 (1981).
- [38] E. J. Janse van Rensburg and N. Madras, A nonlocal Monte Carlo algorithm for lattice trees, *J. Phys. A: Math. Gen.* **25**, 303 (1992).
- [39] D. Landau and K. Binder, *A Guide to Monte Carlo Simulations in Statistical Physics* (Cambridge University Press, New York, 2005).
- [40] M. Newman and G. Barkema, *Monte Carlo Methods in Statistical Physics* (Clarendon Press, Oxford, England, 1999).
- [41] W. Krauth, *Statistical Mechanics: Algorithms and Computations*, ser. EBSCO ebook Academic Collection (Oxford University Press, Oxford, England, 2006).
- [42] P. C. Hohenberg and B. I. Halperin, Theory of dynamic critical phenomena, *Rev. Mod. Phys.* **49**, 435 (1977).
- [43] K. E. Evans and S. F. Edwards, Computer simulation of the dynamics of highly entangled polymers, Part 1.—Equilibrium dynamics, *J. Chem. Soc., Faraday Trans. 2* **77**, 1891 (1981).
- [44] A. van Heukelum and G. T. Barkema, Reaching large lengths and long times in polymer dynamics simulations, *J. Chem. Phys.* **119**, 8197 (2003).
- [45] V. Hugouvieux, M. A. V. Axelos, and M. Kolb, Amphiphilic multiblock copolymers: From intramolecular pearl necklace to layered structures, *Macromolecules* **42**, 392 (2009).
- [46] R. D. Schram, G. T. Barkema, and H. Schiessel, On the stability of fractal globules, *J. Chem. Phys.* **138**, 224901 (2013).
- [47] P. G. de Gennes, Reptation of a polymer chain in the presence of fixed obstacles, *J. Chem. Phys.* **55**, 572 (1971).
- [48] D. Michieletto, On the tree-like structure of rings in dense solutions, *Soft Matter* **12**, 9485 (2016).
- [49] R. Schram and G. Barkema, Simulation of ring polymer melts with GPU acceleration, *J. Comput. Phys.* **363**, 128 (2018).
- [50] A. Rosa and R. Everaers, Conformational statistics of randomly branching double-folded ring polymers, *Eur. Phys. J. E* **42**, 7 (2019).
- [51] B. H. Zimm and W. H. Stockmayer, The dimensions of chain molecules containing branches and rings, *J. Chem. Phys.* **17**, 1301 (1949).
- [52] P.-G. De Gennes, Statistics of branching and hairpin helices for the dAT copolymer, *Biopolymers* **6**, 715 (1968).
- [53] J. Isaacson and T. C. Lubensky, Flory exponents for generalized polymer problems, *J. Phys. Lett.* **41**, 469 (1980).
- [54] M. Daoud and J. F. Joanny, Conformation of branched polymers, *J. Phys.* **42**, 1359 (1981).
- [55] P. J. Flory, *Principles of Polymer Chemistry* (Cornell University Press, Ithaca, New York, 1953).
- [56] M. Rubinstein, Discretized Model of Entangled-Polymer Dynamics, *Phys. Rev. Lett.* **59**, 1946 (1987).
- [57] N. C. Karayiannis, V. G. Mavrantzas, and D. N. Theodorou, A Novel Monte Carlo Scheme for the Rapid Equilibration of Atomistic Model Polymer Systems of Precisely Defined Molecular Architecture, *Phys. Rev. Lett.* **88**, 105503 (2002).
- [58] N. Metropolis, A. W. Rosenbluth, M. N. Rosenbluth, A. H. Teller, and E. Teller, Equation of state calculations by fast computing machines, *J. Chem. Phys.* **21**, 1087 (1953).
- [59] See Supplemental Material at <http://link.aps.org/supplemental/10.1103/PhysRevE.104.014501> for generated videos.
- [60] R. Hess, *Blender Foundations: The Essential Guide to Learning Blender 2.6* (Focal Press, Waltham, MA, 2010).
- [61] K. Binder, Time-dependent Ginzburg-Landau theory of nonequilibrium relaxation, *Phys. Rev. B* **8**, 3423 (1973).
- [62] D. Frenkel and B. Smit, *Understanding Molecular Simulation*, 2nd ed. (Academic Press, Inc., New York, 2001).
- [63] D. Jost, P. Carrivain, G. Cavalli, and C. Vaillant, Modeling epigenome folding: Formation and dynamics of topologically associated chromatin domains, *Nucleic Acids Res.* **42**, 9553 (2014).
- [64] H. J. Herrmann, D. C. Hong, and H. E. Stanley, Backbone and elastic backbone of percolation clusters obtained by the new method of “burning,” *J. Phys. A: Math. Gen.* **17**, L261 (1984).